Journal of Biomedical Optics 11(2), 024009 (March/April 2006)

Fluorescence spectroscopic analysis of surface and subsurface residual stress fields in alumina hip joints

Giuseppe Pezzotti
Kyoto Institute of Technology
Ceramic Physics Laboratory and Research Institute
for Nanoscience
RIN, Sakyo-ku, Matsugasaki
606-8585 Kyoto, Japan

Toshiyuki Tateiwa
Kyoto Institute of Technology
Ceramic Physics Laboratory and Research Institute
for Nanoscience
RIN, Sakyo-ku, Matsugasaki
606-8585 Kyoto, Japan
and
Tokyo Medical University
Department of Orthopedic Surgery
Shinjuku-ku, 6-7-1 Nishishinjuku
160-0023 Tokyo, Japan

Wenliang Zhu
Kyoto Institute of Technology
Ceramic Physics Laboratory and Research Institute
for Nanoscience
RIN, Sakyo-ku, Matsugasaki
606-8585 Kyoto, Japan

Tsuyoshi Kumakura
Kyoto Institute of Technology
Ceramic Physics Laboratory and Research Institute
for Nanoscience
RIN, Sakyo-ku, Matsugasaki
606-8585 Kyoto, Japan
and
Tokyo Medical University
Department of Orthopedic Surgery
Shinjuku-ku, 6-7-1 Nishishinjuku
160-0023 Tokyo, Japan

Kiyotaka Yamada
Kyoto Institute of Technology
Ceramic Physics Laboratory and Research Institute
for Nanoscience
RIN, Sakyo-ku, Matsugasaki
606-8585 Kyoto, Japan

Kengo Yamamoto
Tokyo Medical University
Department of Orthopedic Surgery
Shinjuku-ku, 6-7-1 Nishishinjuku
160-0023 Tokyo, Japan

Abstract. We aim to establish a confocal spectroscopic technique able to study the features of fluorescence spectra arising from native Cr^{3+} impurity in polycrystalline alumina (Al_2O_3) as a biomaterial and to use their emission lines as microscopic probes for the characterization of residual stress fields stored in artificial hip prostheses during their implantation *in vivo*. As an application of the technique, we report for the first time concerning the evolution of microscopic (residual) stress fields stored on the surface and in the subsurface of $N=7$ retrieved Al_2O_3 hip joints after exposure in the human body from a few months to 19 yr. The micrometric diameter of the laser beam waist impinging on the joint surface (typically about 1 μm in lateral resolution) enables us to estimate the patterns and magnitude of residual stress with high spatial resolution, at least comparable with the grain size of the material. In addition, a selected confocal configuration for the optical probe enables minimization of the probe size along the in-depth direction. According to a statistical collection of data on the microscopic level for retrieved femoral heads *in toto*, a residual stress field arising from loading history *in vivo* during the lifetime of the Al_2O_3 femoral head can be revealed. Finally, an interpretation is given of microscopic wear mechanisms in Al_2O_3 artificial hip joints consistent with the observed evolution of surface residual stress fields on elapsed time *in vivo*. [DOI: 10.1117/1.2193470]

Keywords: confocal fluorescence spectroscopy; alumina; artificial hip joint; residual stress; probe response function.

Paper 05296R received Oct. 6, 2005; revised manuscript received Dec. 21, 2005; accepted for publication Dec. 22, 2005;

1 Introduction

Confocal laser spectroscopy is a useful technique for the analysis of material surfaces because, after appropriate calibration, it may enable one not only to screen the very surface of the material but also to perform nondestructively in-depth scanning along the *z* axis (i.e., the axis perpendicular to the specimen surface) with relatively high spatial resolution.[1,2] Confocality-aided spectroscopic assessments can be dedicated to the quantitative analysis of residual stresses (a technique referred to as confocal piezospectroscopy, henceforth) stored on the material surface. This technique was recently applied

---

Address all correspondence to Giuseppe Pezzotti, Kyoto Institute of Technology, Department of Materials, Sakyo-ku, Matsugasaki — Sakyo-ku, Kyoto, Kyoto-hu 606–8585 Japan. Tel: 81–75–724–7568; Fax: 81–75–724–7568; E-mail: pezzotti@kit.ac.jp

1083-3668/2006/11(2)/024009/10/$22.00 © 2006 SPIE

to the micromechanical characterization of zirconia hip joints after *in vitro* testing or retrieval from human body.[3] The (lateral) micrometer spatial resolution that is available for piezospectroscopic stress measurements makes the technique particularly suitable for the assessment of stress distributions that vary rapidly and significantly within small material volumes. Surface deterioration on wear of the ceramic femoral heads after total hip arthroplasty is indeed one of these cases, and therefore, is a typical biomedical item that can be quantitatively studied on a microscopic level by means of confocal piezospectroscopic assessments.[3–5] The wear rate of the surface, environmentally assisted by the complex interaction between the femoral head and its holding acetabular cup, may strongly depend on the microstructural characteristics of the ceramic material and, in particular, on the microscopic residual stress state preexisting on the microtructural level. Note, in this context, that wear-related phenomena and thus residual stresses are maximized on the head surface and vary rapidly with position along the z axis.

Alumina bearing surfaces were introduced in the seventhies in hip joint arthroplasty after laboratory tests and simulator studies demonstrated the low friction and wear of alumina prostheses.[6,7] However, today concerns remain about their long-term performance *in vivo*, despite published clinical studies that have already established the safety and the good tribological performance of this material. The most common reason for revision has been loosening of the joint, but the mechanisms that have led to this loosening have not yet been satisfactorily explained.[8] In other words, it is still unclear what role wear and wear debris play in the long-term performance of the alumina hip joint or indeed if wear is a factor in the loosening process. In the complex background of this problem, our understanding is that, although all alumina hip joints are usually classified within the same category of material, the polycrystalline nature of the material may make both the observed properties and performance very scattered. In particular, the grain size of polycrystalline alumina, which is directly related to the manufacturing process, likely plays a fundamental role in the tribological behavior of the material.

In this paper, we propose a set of calibration assessments aimed to establish the quantitative use of the confocal piezospectroscopic technique in Al_2O_3 bioceramics and apply it to rationalize the complex evolution *in vivo* of the microscopic residual stress fields stored on the surface of alumina hip joints. In particular, it is shown that monitoring (with the aid of a confocal probe) the piezospectroscopic behavior of the fluorescence doublet arising from native Cr^{3+} impurity in Al_2O_3 enables the reliable quantitative characterization of residual stress fields both on the surface and in the subsurface of the artificial hip joint. Residual stresses play a major role in surface deterioration on wear, and spectroscopic principles are relevant to understand surface deterioration phenomena in retrieved alumina femoral heads and the causes behind the failure of artificial joints. We believe that the understanding achieved through precise spectroscopic assessments will ultimately enable the replacement of empirical optimizations for biomaterials processing with more systematic procedures, thus greatly speeding the development of hip joints with improved reliability.

Table 1 List of retrieved Al_2O_3 femoral heads with their respective maker, grain size, and implantation time *in vivo*.

	Implantation Time	Grain Size (μm)	Material Type/ Brand	Generation
Case 1	1 month	2	Biolox Forte	III
Case 2	1 y 3 months	2	Biolox Forte	III
Case 3	1 y 7 months	4	Unknown	II
Case 4	2 y 6 months	2	Biolox Forte	III
Case 5	6 y 8 months	5.5	Unknown	II
Case 6	17 y	9	Mittelmeyer	I
Case 7	19 y	7	Ceraver	1

2 Materials and Methods

2.1 *Materials*

A total of seven retrieved Al_2O_3 ceramic femoral heads were studied, which were revised after short, medium, or long-term periods of *in vivo* implantation in patients (Table 1). All these prostheses were retrieved after a successful use in patients. However, all the implants underwent aseptic or septic, stem or cup, loosening. Among the seven cases discussed here, only case 6 (cf. Table 1) was a femoral head of the “mushroom-type;” the other six balls were of the usual truncated spherical shape, without any ceramic skirt to partially cover the metallic stem. The heads are classified in Table 1 as first- to third-generation Al_2O_3 according to the manufacturing year; the most recently fabricated heads were defined as the third generation. All the analyzed femoral heads were employed against polyethylene acetabular cups. After retrieval and sterilization, the grain size of each ball was measured on scanning electron micrographs (JEOL-6500F, JEOL, Tokyo, Japan) using the linear intercept method; at least 500 grains were measured for each ceramic head. The average grain size is also reported in Table 1. More details about the clinical history of the implants have been reported elsewhere.[9,10]

2.2 *Piezospectroscopic Assessments*

Fluorescence spectra were collected with a triple monochromator spectrometer (T-64000, ISA Jovin-Ivon/Horiba Group, Tokyo, Japan) equipped with a charge-coupled detector (high-resolution CCD camera). In mapping residual stress fields, the required laser power on the Al_2O_3 surface was typically about 200 mW at the laser head and a suitable excitation frequency was a monochromatic blue line emitted by an Ar-ion laser at a wavelength of 488 nm. The spectral integration time was typically 1 s, with averaging the recorded spectra over three successive measurements. All the spectra were recorded at room temperature. The optical microscope was connected to a video monitor that enabled scanning of the sample surface to locate the selected location for the spectroscopic measurement. The wave numbers of fluorescence band maxima were obtained by fitting the CCD raw data to mixed Gaussian/Lorentzian curves with commercially available software. Alumina femoral heads were placed on a mapping device (lateral

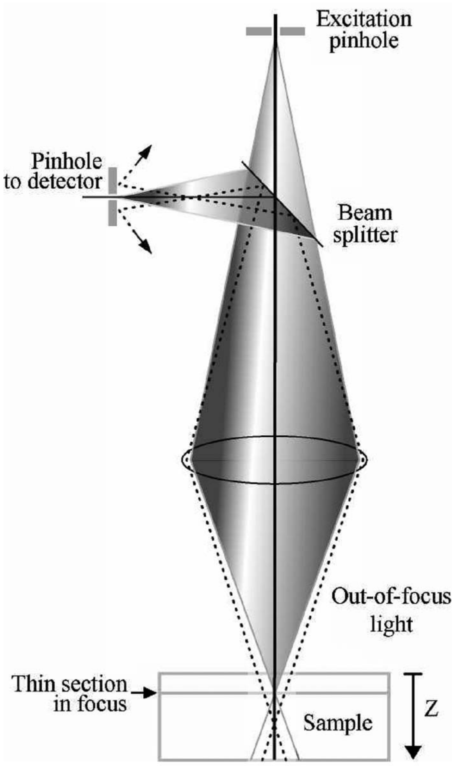

Fig. 1 Schematic of the optical probe in confocal configuration.

resolution of 0.1 μm), which was connected to a personal computer to drive highly precise displacements (along both x and y axes) on the sample. Given the curved nature of the investigated surfaces, an autofocus device was adopted throughout automatic mapping experiments. Confocal experiments were conducted with focusing the waist of the laser beam either on the surface or on subsurface planes of the artificial joint through an optical lens ($\times 100$). Then, the fluorescence signal was refocused onto a small confocal (pinhole) aperture that acted as a spatial filter, passing the signal excited at the beam waist, but substantially eliminating fluorescence signals produced at other points above and below the beam waist. The filtered signal then returned to the spectrometer (via the probe head) where it was dispersed onto the CCD camera to produce a spectrum. In practice, a pinhole aperture was placed in the optical train of the microprobe spectrometer and used to regulate the rejection of out-of-focus light. Confocal microscopy was used to probe selected xyz locations in the samples, with micrometer (lateral) spatial resolution. Two-dimensional data maps were built by xy scanning the sample, and 3-D data sets were produced by sequentially acquiring a set of xy slices at different z depths. A schematic of the confocal probe configuration is given in Fig. 1.

The dependence of the chromophoric bands of Al_2O_3 on stress has been amply documented in the literature.[11–13] However, to minimize possible errors deriving from the use of a different probe with respect to literature data, a complete set of piezospectroscopic calibrations was newly performed both on polycrystalline Al_2O_3 (with different grain sizes) and single-crystal sapphire. This calibration set enabled us to check the consistency of the measured residual stress data and to assess the error involved with our stress measurements in polycrystalline materials. As for the calibration procedure, a ceramic bar was mounted on a four-point bending jig and placed under the optical microscope. Load was applied and the whole jig was moved under the optical microprobe to record spectra every 50 μm along the specimen thickness. The applied load was converted into a stress distribution using the standard four-point bending elastic beam equation and the recorded spectral shifts of the fluorescence bands were plotted as a function of elastic stress. The slope Π_{av} of stress/shift plots in Al_2O_3 polycrystals was precisely recorded and used throughout assessments of unknown residual stress fields. As far as elastic stress fields were concerned, applied stresses recorded along a line perpendicular to the long axis of the bending bar (i.e., along the thickness at the center of the bar) could be regarded as uniaxial stresses and linearly changing from a compressive to a tensile magnitude (at the sides of the small and of the large span of the four-point bending bar configuration, respectively).

3 Theoretical Background

3.1 *Piezospectroscopic Principles*

The piezospectroscopic (PS) method has been widely used for the microscopic evaluation of residual stresses in single and polycrystalline ceramics.[11–13] The characterization is based on the precise evaluation of the spectral shift ($\Delta\omega = \omega - \omega_0$) occurring in the stressed material (with band maximum located at ω) with respect to its unstressed status (with band maximum at ω_0). The following (tensorial) PS equation can be used for single-crystal materials, irrespective of whether the selected spectroscopic band arises from an electronic transition (fluorescence band) or from a lattice vibrational mode[14] (Raman band):

$$\Delta\omega = \Pi_{ij}\sigma_{ij} = \Pi^*_{ii}\sigma^*_{jj} \quad (i,j = 1, 2, 3), \tag{1}$$

where σ_{ij} is the stress tensor existing in the probed volume, and Π_{ij} is a second-rank tensor (i.e., the tensor of the PS coefficients). An asterisk to the stress tensor denotes the choice of a set of Cartesian axes coincident with the principal stress directions, while an asterisk to the tensor of PS coefficients denotes the coincidence of the preceding system of Cartesian axes with the principal axes of the crystal. Note that Eq. (1) also shows that the observed spectral shift is an invariant with respect to the selected system of coordinates. In polycrystalline materials with a random orientation of the grains, the PS coefficient is independent of direction and can be taken as an average value along all the crystallographic directions. Considering the hexagonal symmetry of the Al_2O_3 single crystal, the average PS coefficient Π_{av} for an Al_2O_3 polycrystal can be represented as follows:

$$\Pi_{av} = \frac{\Pi_{11} + \Pi_{22} + \Pi_{33}}{3} = \frac{2\Pi_a + \Pi_c}{3}, \tag{2}$$

where the subscripts a and c denote the principal crystallographic axes of the hexagonal Al_2O_3 lattice cell (which shows symmetry with respect to the plane perpendicular to the c axis). Therefore, for a general triaxial stress state, $\sigma_{ij} \equiv \sigma^*_{jj}$, applied to a polycrystalline sample, Eq. (1) can be simplified to a scalar proportionality equation:

$$\Delta\omega = \Pi_{\mathrm{av}}\langle\sigma_{jj}^{*}\rangle, \tag{3}$$

where $\langle\sigma_{jj}^{*}\rangle$ is the trace of the principal stress tensor. In other words, a measurement of spectral shift gives direct access to the trace stress tensor stored in the probed volume. In addition, the nature of the stress trace can also be deduced from the positive or negative sign of $\Delta\omega$ (in the case of tensile or compressive stress, respectively, for both chromophoric bands of alumina). Note that, even in a nominally "stress-free" polycrystalline Al_2O_3, a (microscopic) residual stress field (mainly arising from anisotropy in thermal expansion along different crystallographic axes) is developed. The stress state on the microstructural scale in polycrystalline Al_2O_3 ceramics was intensively studied using the PS method.[11–13] The spatial distribution on the scale of the grain size obeys a statistical distribution, which strongly depends on the average grain size of the polycrystal; however, the average value of this thermal stress distribution should be zero when a large number of grains are sampled. A full treatment of PS characteristics in polycrystalline Al_2O_3 was given by Ma and Clark;[13] here, only PS notions that are salient to the interpretation of the fluorescence spectral characteristics of Al_2O_3 hip joints in terms of residual stress fields are reported.

3.2 *Probe Response Function*

In photostimulated spectroscopy, it can be assumed that each point in the irradiated volume (x,y,z) gives rise to a optical (scattered) intensity contribution to the spectrum that obeys a given statistical distribution (e.g., Lorentzian). The observed fluorescence spectrum depends on the intensity distribution of scattered light around the irradiation point. This intensity distribution is called the probe response function $B(x,y,z,x_0,y_0,z_0)$ of the light scattered from the point (x,y,z) when the incident beam is focused on the point[15,16] (x_0,y_0,z_0):

$$B(x,y,z,x_0,y_0,z_0) \propto \exp\left[-\frac{(x-x_0)^2+(y-y_0)^2}{2R^2}\right] \times \frac{p^2}{(z-z_0)^2+p^2}\exp(-2\alpha z), \tag{4}$$

where $2R$ is the laser beam diameter in the focal plane, p is the probe response parameter (for an unfocused beam, p tends to infinity), and α is the absorption coefficient of the material at the incident wavelength. For fluorescence bands, the incident photons and emitted photons may have remarkably different energies and absorption coefficients, therefore the probe response function should be experimentally determined case by case. According to this observation, the term 2α in Eq. (4) may need to be substituted for by the sum of the absorption coefficients for incident and emitted light. The observable spectrum intensity can be then obtained according to the following volumetric integration:

$$I_{\mathrm{obs}}(\omega_p) \propto \int_{-\infty}^{\infty} \mathrm{d}x \int_{-\infty}^{\infty} \mathrm{d}y \int_{-\infty}^{\infty} B(x,y,z,x_0,y_0,z_0)\,\mathrm{d}z, \tag{5}$$

where ω_p is the wave number at the maximum of the selected spectral band. In this paper, we restrict our considerations to the in-depth probe response function, thus neglecting any in-plane variation, although the approach followed here is general and can be also extended to the assessment of probe geometry in the focal plane. Supposing, in first approximation, that all the variables in the xy plane can be ignored, a simplification of Eq. (5) can be given as follows[15]:

$$I_{\mathrm{obs}}(\omega_p) \propto \int_{-\infty}^{\infty} \exp(-2\alpha z)\frac{p^2}{p^2+(z-z_0)^2}\,\mathrm{d}z, \tag{6}$$

where the focal plane position (above or below the sample surface) z_0 can be also seen as a defocusing distance with respect to irradiation with the focal plane placed on the sample surface. In highly transparent materials (e.g., single-crystalline Al_2O_3), there is almost no absorption ($\alpha \approx 0$). Using the maximum observed intensity to normalize spectral intensity, Eq. (6) can be integrated analytically to give

$$\frac{I_{\mathrm{obs}}(\omega_p)}{I_{\mathrm{obs,max}}(\omega_p)} = \frac{1}{2} - \frac{1}{\pi}\arctan\left(-\frac{z_0}{p}\right), \tag{7}$$

where $I_{\mathrm{obs,max}}$ is the maximum observed intensity of the selected band of the spectrum on varying defocusing distance z_0. When the absorption coefficient is appreciably different from zero, the maximum intensity cannot be observed experimentally. In this case, we assumed: $I_{\mathrm{obs,max}}=2I_{\mathrm{obs,sur}}$, where $I_{\mathrm{obs,sur}}$ is the observed intensity when the focal plane is placed on the sample surface. This value was used to normalize the calculated intensity, as follows:

$$\frac{I_{\mathrm{obs}}(\omega_p)}{I_{\mathrm{obs,max}}(\omega_p)} = \frac{\int_{-\infty}^{\infty} \exp(-2\alpha z)\left[\frac{p^2}{p^2+(z-z_0)^2}\right]\mathrm{d}z}{2\int_{0}^{\infty} \exp(-2\alpha z)\left(\frac{p^2}{p^2+z^2}\right)\mathrm{d}z}. \tag{8}$$

Note that in this case, no analytical integration is possible and Eq. (8) must be integrated numerically. As the probe is swept along the in-depth axis, the collected intensity function I_{obs} maps the probe response. The probe response parameter p and the absorption coefficient α can be obtained then from the best fitting of the (normalized) experimental intensities to the calculated ones [according to Eq. (7) or (8)]. This method to determine the probe function through changing the focal plane is referred to as the defocus method. To visualize the probe size in terms of penetration depth, a probe depth z_d can be defined according to the following equation (using 90% of the maximum intensity as a threshold value):

$$\frac{\int_0^{z_d} B(z,z_0)\mathrm{d}z}{\int_0^{\infty} B(z,z_0)\mathrm{d}z} = 0.9. \tag{9}$$

Note that this equation is valid only for fully transparent materials, whose absorption coefficient is zero; a solution to this equation can be given in finite terms, as follows:

$$z_d = z_0 + p \tan\left(0.45\pi - 0.1 \arctan \frac{z_0}{p}\right). \tag{10}$$

Therefore, when the laser waist is focused on the surface ($z_0=0$), the depth probed by a given spectral band can be calculated according to Eq. (10). Most of the equations in this paper were solved with the aid of a commercially available computational software package.[17]

3.3 *Probe Response Function in Confocal Probe Configuration*

The combination of an optical microprobe and a motorized x, y, and z stage enables the generation of 2-D or 3-D maps that can yield information on the distribution of stress fields in heterogeneous samples. However, the laser penetration depth in transparent or semitransparent materials (e.g., polycrystalline Al_2O_3) can be fairly large, which in turn may induce a large probe convolution. A strategy to improve in-depth resolution consists of placing a confocal pinhole at the back-focal-image plane to partly cut off the light scattered from outside the laser focal area (i.e., greatly reducing the effect of probe depth). By employing this technique, referred to as "confocal spectroscopy," it is possible to probe discrete z planes with relatively high in-depth spatial resolution.

When a laser is focused on the specimen surface ($z_0=0$), an inner transmitted zone exists for the scattered/emitted light within a solid angle $\theta \leqslant \theta_{tr}$ varying as a function of the depth position z. The collection solid angle Ω, which takes into account the competitive effects of the numerical aperture (NA) of the objective lens and of the pinhole aperture, can be expressed as follows:

$$\Omega = 2\pi(1-\theta_{tr}) = \begin{cases} 2\pi\left[1 - \dfrac{z}{(z^2+\rho_0^2)^{1/2}}\right] & (\rho_{max} \geqslant \rho_0) \\ 2\pi\left[1 - \dfrac{z}{(z^2+\rho_{max}^2)^{1/2}}\right] & (\rho_{max} \leqslant \rho_0), \end{cases} \tag{11}$$

$$z = \rho_{max}\left[(n^2-1) + \left(\frac{f}{D/2-\rho_{max}}\right)^2 n^2\right]^{1/2}, \tag{12}$$

where ρ_{max} is the maximum transverse ray aberration from the optical axis (determined by the NA of the objective lens); the confocal pinhole with diameter Φ has a virtual back-image $2\rho_0$ in the sample focal plane given by the relation $\Phi = 2\rho_0 \mathrm{MP}G$, where MP is the magnification power of the objective and G is the enlargement factor (1.4); note that only light from within the virtual circle $2\rho_0$ on the surface can pass through the pinhole; n is the refractive index of the material, and D/f is the diameter/focal length of the objective lens. For any given z value, ρ_{max} can be derived from Eq. (12). The collection solid angle remains almost invariant near the surface; then, it falls pronouncedly because of the blinding effect of the confocal pinhole aperture, the smaller the pinhole aperture the more abrupt the Ω drop-down. With reducing the diameter of the pinhole aperture, Φ, the subsurface depth z, at which the Ω value begins to drop significantly, gradually approaches the surface. A parameter representative of the penetration depth of the laser probe in a given confocal configuration is the threshold value of the in-depth abscissa t below which the collection solid angle abruptly drops down:

$$t = \rho_0\left[(n^2-1) + \left(\frac{f}{D/2-\rho_0}\right)^2 n^2\right]^{1/2}. \tag{13}$$

In principle, the probe depth can be pushed down to a single micrometer by reducing the diameter of the pinhole aperture. However, a significant drop-down in the efficiency of the collected spectrum with reducing Φ greatly limits the achievable in-depth resolution. In practice, millimeter scale mapping of the artificial joint surface with micrometric spatial resolution requires the acquisition time for a single spectrum to be set to a few seconds or less. This limitation involves minimum pinhole apertures to be selected in the range $20 \leqslant \Phi \leqslant 100\ \mu\mathrm{m}$ for Al_2O_3 ceramics. Equation (13) is strictly valid only for $z_0=0$, while error is involved when the focal plane is shifted along the subsurface of the sample, the larger z_0, the larger the error. However, an estimate of probe depth made through Eq. (13) represents an upper limit for probe size at a given pinhole aperture for a selected sample. As for the observed intensity I_{obs} in a confocal probe configuration with the focal plane placed on the sample surface, an equation similar to Eq. (6) holds, as follows:

$$I_{obs}(\omega_p) \propto \int_0^t \Omega(\rho_{max} \leqslant \rho_0)\exp(-2\alpha z)\frac{p^2}{z^2+p^2}\mathrm{d}z + \int_0^{\infty} \Omega(\rho_{max} \geqslant \rho_0)\exp(-2\alpha z)\frac{p^2}{z^2+p^2}\mathrm{d}z. \tag{14}$$

Equation (14), which can be eventually normalized by the maximum spectral intensity as made for Eq. (6), will be used to analyze the configuration of the confocal probe in the Al_2O_3 materials. Note, however, that in polycrystalline materials, inhomogeneous scattering may occur, mainly due to the effect of grain boundaries. In this case, the collection solid angle Ω in Eq. (14) should be replaced by the collection cross section S_z:

$$S_z = \Omega\Psi = \Omega A e^{Bz+C} = \Omega A' \exp(\alpha_{eff} z), \tag{15}$$

where A, A', B, and C are numerical parameters (with $A' = Ae^C$). Note that the condition $\Psi = 1$ applies only for media with homogeneous emission/scattering. Incorporating the exponential term from Eq. (15) into the absorption exponential term in Eqs. (6) and (14), we can introduce an effective absorption coefficient α_{eff} that takes into consideration both incident and emitted photons with their respective energies and

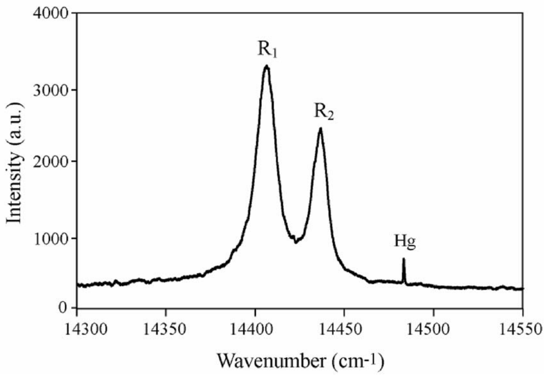

Fig. 2 Typical spectrum of polycrystalline Al_2O_3 arising from the native presence of Cr^{3+} impurities substitutional to Al^{3+}.

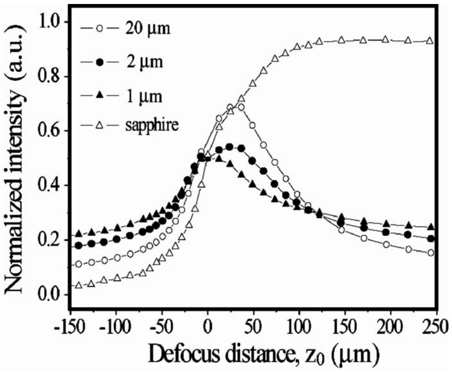

Fig. 3 Probe response functions for single-crystal sapphire and for Al_2O_3 polycrystals with different (average) grain sizes.

absorption coefficients, and formally leave the equations as stated (but with $\alpha=\alpha_{\mathrm{eff}}$). When the confocal pinhole is set to a given aperture, we can calculate the probe depth z_d by solving the following equation:

$$\frac{\int_0^{z_d} S(z,\rho_0)B(z)\mathrm{d}z}{\int_0^{\infty} S(z,\rho_0)B(z)\mathrm{d}z}=0.9, \tag{16}$$

which is conceptually similar to Eq. (9) (with $z_0=0$).

4 Results and Discussion

4.1 *Confocal Probe Geometry and PS Calibrations*

A typical fluorescence spectrum from a polycrystalline Al_2O_3 material, consisting of the chromophoric doublet R_1 and R_2 (ruby lines), is shown in Fig. 2. Spectra were collected from Al_2O_3 polycrystals with different grain sizes, but they appeared the same as that shown in Fig. 2, which refers to a polycrystal with average grain size of 2 μm. Note that, despite the relatively intense fluorescence signal retrieved in spectroscopic assessments, the content of Cr^{3+} ion as a natural impurity in the Al_2O_3 crystalline lattice is usually confined to a range[18,19] <60 ppm. In this study, no Cr^{3+} ions or Cr-related compounds were intentionally added to the investigated alumina materials, so the Cr impurity range was substantially small and no significant spectral shift related to chemical composition was expected in that range.[20] Although the origin of the ruby spectrum has been fully described by other authors,[21,22] we briefly describe here the related probe response function (in confocal probe configuration) as a function of grain size (in comparison with that of single-crystal sapphire). A full description of the evolution of the probe response function of polycrystalline Al_2O_3 with increasing grain size has not yet been reported in the literature. The intensity of the ruby doublet lines was collected as a function of defocus displacement z_0 along the in-depth direction perpendicular to the sample surface. A complete coincidence was observed in the optical behaviors of the R_1 and R_2 fluorescence bands. Therefore, only the R_1 band is discussed henceforth. The experimental (normalized) R_1 intensity trends (i.e., the probe response functions) are shown in Fig. 3 as collected in polycrystals with different grain size. From these data, we can see that significant difference exists in the defocusing behavior of polycrystals when the grain size is altered. In particular, the finer the grain size, the more the probe response function differed from that of fully transparent sapphire, thus gradually changing from a completely sigmoidal trend (typical of highly transparent materials) to a bell-shaped function (characteristic of opaque materials). The parameters selected for best-fitting the probe response functions were determined by solving Eqs. (6) and (14) for normal and confocal ($\times$100

Table 2 Optical characteristics of confocal and nonconfocal probes and PS characteristics in single-crystal sapphire and Al_2O_3 polycrystals with different grain sizes.

Material/ Grain Size	p (μm)	α_{eff} (μm^{-1})	z_d (μm) (Nonconfocal)	z_d (μm) (Confocal)	Π_{av} (cm^{-1}/GPa)	R^2
Sapphire	20	≈0	126	15	$\Pi_{av}=\frac{2\Pi_n+\Pi_c}{3}=2.54$	0.998
Al_2O_3/20 μm	51	0.006	81	5	2.530	0.985
Al_2O_3/2.0 μm	75	0.018	50	2.7	2.625	0.990
Al_2O_3/1 μm	90	0.14	9	1.6	2.665	0.996

objective lens, NA=0.9, $\Phi=100$ μm, and $f=0.3$ mm) probe configurations, respectively, are shown in Table 2, together with the probe depth z_d calculated according to Eqs. (9) and (16) for through-focus and confocal probe configurations, respectively. In the case of sapphire ($\alpha_{\text{eff}}\approx 0$), the probe geometry evaluation was made according to Eq. (10). With decreasing grain size, the values of p and α_{eff} increased, and the probe depth decreased accordingly. Clearly, the probe geometry is strongly influenced by the area of grain boundary per unit volume present in the polycrystalline matter, which increases with decreasing grain size. In other words, the presence of light multireflections, refractions, and scattering at grain boundaries can strongly influence the material absorption through the dissipation of photon energy. One important implication in these findings is that fluorescence spectra collected by nonconfocal probe configuration in polycrystalline samples with different grain size may average spectral information from different portions of subsurface. Accordingly, the differences in measured residual stress values can be very pronounced, especially in the presence of large property gradients along the sample subsurface. In this context, it seems to be mandatory to know the grain size of the Al_2O_3 material of which the artificial joint is made, to correctly interpret residual stress data collected by PS techniques. Note also that, although smaller than in the case of a sapphire single-crystal, the probe penetration depth z_d along the subsurface in coarse-grained Al_2O_3 polycrystals in a nonconfocal probe configuration can be as large as 80 μm, although it greatly reduces to 9 μm in a finely grained material. On the other hand, when a confocal probe configuration is adopted, the probe size greatly reduces with respect to its depth, the smaller the grain size of the Al_2O_3 polycrystal, the smaller the probe depth. The probe penetration depth can be reduced to values as small as ≈ 2 μm in fine-grained Al_2O_3. Polycrystals with coarse and medium grain sizes greatly benefit from the use of a confocal probe in terms of probe size reduction. In conclusion, it seems to be more appropriate to use a confocal probe to evaluate the expectedly strongly graded residual stress fields stored near the surface of retrieved Al_2O_3 artificial hip joints. Since the slice of material subsurface contributing to the spectrum (taken at a given focal abscissa z_0) can be significantly reduced by collecting the scattered light in a confocal probe configuration, it seems to be a possible minimization of convolutive effects on the measured magnitude of residual stress.

The uniaxial PS coefficient Π_{av} of the R_1 band was evaluated to be in the range between 2.53 and 2.66 $\text{cm}^{-1}/\text{GPa}$ for all the grain sizes investigated in this study (these values are consistent with those reported in previous studies[23]). Table 2 shows the results of the Π_{av} values (and the respective correlation factors to a linear fit, R^2) obtained by four-point bending calibration for different Al_2O_3 polycrystals. Here R_1 was the spectroscopic band of Al_2O_3 that showed the maximum stress sensitivity and it is used throughout the residual stress assessments. The uniaxial PS coefficient was transformed into a hydrostatic one (appropriate for residual stress assessments) according to the simple equation: $\Pi_{\text{hyd}}=3\Pi_{\text{av}}$. Consistency between measurements on single-crystalline and polycrystalline samples was found according to the following considerations (cf. Table 2). When the material shows a random distribution of grain orientation and provided that a statistically meaningful grain sampling is made in the stress assessment, the PS coefficient for an Al_2O_3 polycrystal Π_{av} can be related to those of a sapphire single-crystal collected on different crystallographic planes, according to Eq. (2). As can be seen in Table 2, the agreement was satisfactory for all the investigated polycrystals within a confidence of a few percent. In this context, we noticed a decrease in data scatter in polycrystals with finer grain sizes, which arose from the larger number of grains sampled (and thus to a sampling closer to statistically invariant conditions) in the probed volume. Finally, note that the calibration in the bending bar configuration was scarcely affected by the penetration depth of the laser probe, because the stress distribution on the side of the bending bar is independent of the in-depth direction. The calibration procedures described in this section represent the basis for the quantitative evaluation of residual stress fields in retrieved Al_2O_3 artificial hip joints presented in the remainder of this paper.

4.2 *Residual Stress Fields in Retrieved Al_2O_3 Artificial Joints*

As a first-screening characterization to reveal the overall stress patterns with a statistically meaningful sampling, residual stress analysis was performed *in toto* over the entire surface of the femoral heads. The confocal configuration of the probe (×100 objective lens, NA=0.9, $\Phi=100$ μm, and $f=0.3$ mm) was employed throughout the characterization. Figures 4(A) and 4(B) show the maps of residual stress collected on the entire surface of a first-generation femoral head retrieved after long-term implantation (case 7 in Table 1) by placing the focal plane exactly at the sample surface and 30 μm below the surface, respectively. Two main areas could be recognized in which mainly compressive stresses were stored on the load-bearing surface of the ball [cf. Fig. 4(A)]. Interestingly, these areas corresponded to the main wear zones classified on scanning electron micrographs by Shishido et al.[9] on the same femoral head (this item is discussed in detail in the next section). Compressive residual stresses are supposed to arise from the combined long-term actions of wear and of the impingement of the body weight on the bearing surface. When the probe was shifted toward the subsurface [cf. Fig. 4(B)], the residual stresses in the same areas turned out to be tensile in nature. This phenomenon can be explained by considering the static equilibrium that must be established between sample surface and subsurface, which necessarily requires the development of stress fields with opposite signs. The high stress gradient between the sample surface and the subsurface may trigger surface degradation with grain detachment and subsequent formation of ceramic (grain) debris. A significantly different trend was found by screening in toto two third-generation femoral heads retrieved after short-term implantation in human body (cases 1 and 4 in Table 1). On the implant surface, the magnitude of the residual stress field was not only, as expected, significantly lower than that observed in the long-term exposed first-generation femoral heads but also tensile in nature [cf. Figs. 5(A) and 5(B)] for surface residual stresses in cases 1 and 4, respectively]. As a general trend, the (average) residual stress stored on the wear-zone surface of retrieved balls was increasingly tensile up to 1 to 2 yr exposure *in vivo*, then for implants subjected to longer exposure

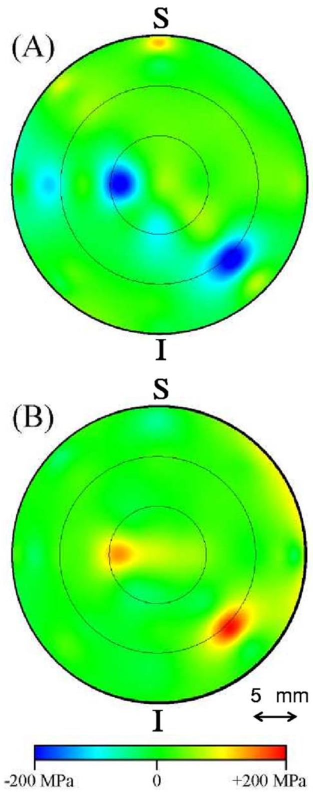

Fig. 4 Residual stress patterns as collected on an Al_2O_3 femoral head (case 7 in Table 1) after long-term exposure *in vivo*: (A) residual stress on the head surface and (B) residual stress state at 30 μm in the subsurface. The letters S and I indicate the superior and the inferior locations, respectively, of the joint during *in vivo* implantation.

times in a human body, residual stress fields in the wear zone were first annihilated and then progressed toward compressive values (cf., average stress magnitudes in the wear zone reported in Fig. 6 as a function of *in vivo* exposure time). The topographic location of areas of stress intensification was not the same for all the retrievals (e.g., compare Figs. 4 and 5). However, this was considered to be the consequence of the different design of the joints and, thus, to arise from different impingement conditions taking place during implantation. Nevertheless, surface residual stress fields showed a trend whose origin should reside in the mechanical interaction between the surfaces of the femoral head and the acetabular cup. Based on the current observation of stress patterns, we propose that both shock and impingement of the acetabular cup on the femoral head introduce on the ceramic surface a residual stress field whose nature changes from tensile in the short-term to compressive in the long-term exposure *in vivo* and whose highest magnitude is reached after significant long-term exposures. The neat magnitude of this residual stress field, henceforth referred to as loading history stress field, was obtained by subtracting the (average) residual stress value recorded from the respective nonwear zones (considered to be representative of the residual stress field preexisting in the femoral head before implantation and thus arising from manufacturing) from the (average) stress field recorded in the main wear zone.

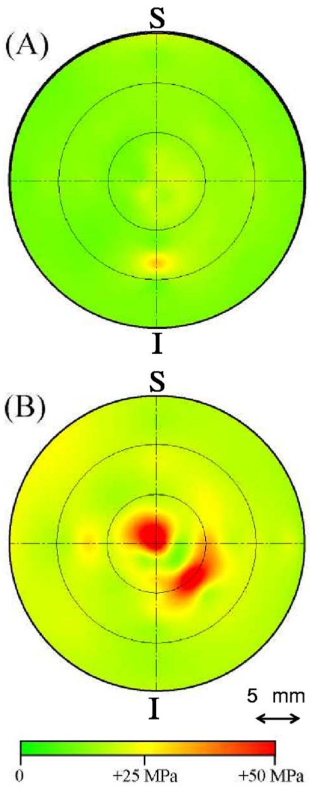

Fig. 5 Residual stress patterns as collected on two short-term exposed Al_2O_3 femoral heads [cases 1 and 4 from Table 1 in (A) and (B), respectively]. The letters S and I indicate the superior and the inferior locations, respectively, of the joint during *in vivo* implantation.

Figures 7(A)-7(D) are typical residual stress maps collected in confocal probe configuration ($\times 100$ objective lens, NA=0.9, $\Phi=100$ μm, and $f=0.3$) with the focal plane placed on the sample surface. In Figs. 7(A) and 7(B), the macro- and microscopic residual stress patterns collected in main wear zones are compared for a third-generation Al_2O_3 prosthesis, respectively. On the other hand, Figs. 7(C) and 7(D) represent the macro- and microscopic residual stress pat-

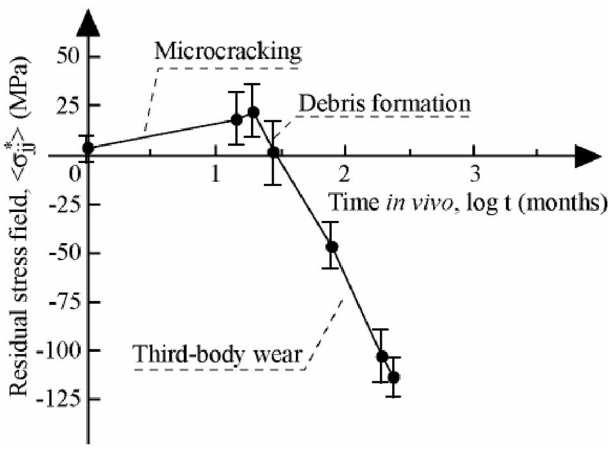

Fig. 6 Plot of the measured (average) residual stress field $\langle \sigma_{jj}^{*} \rangle$ in the main wear zone of Al_2O_3 retrieved femoral heads as a function of the elapsed time *in vivo*.

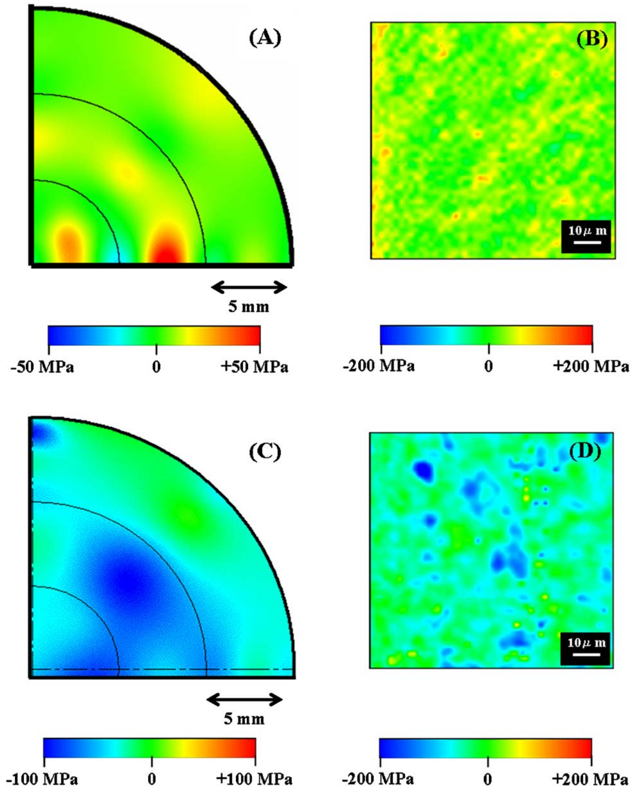

Fig. 7 Macroscopic and microscopic residual stress patterns as revealed by confocal PS on the surface of main wear zone in short-term [(A) and (B), respectively; implanted for 19 months and belonging to the second generation alumina hip joints] and long-term [(C) and (D), respectively, implanted for 204 months and belonging to the first-generation alumina hip joint] exposed Al_2O_3 femoral heads (cases 3 and 6 in Table 1, respectively).

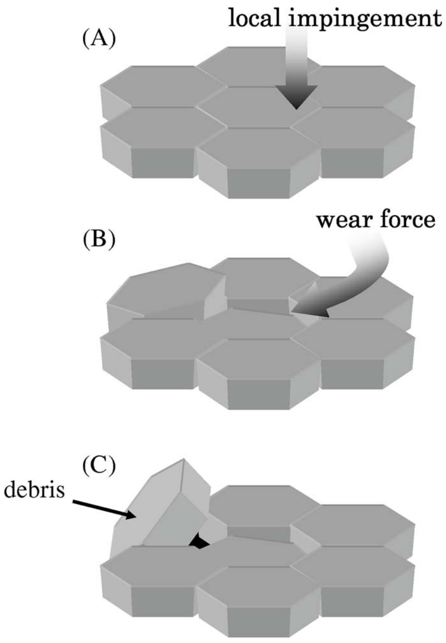

Fig. 8 Schematics of microscopic mechanisms of wear degradation taking place on the surface of Al_2O_3 hip joints *in vivo*.

terns collected in main wear zones in a first-generation Al_2O_3 prosthesis, respectively. It clearly appears that, besides the different size of the wear damage, the average residual stress magnitude in the main wear zone of the third-generation ceramic head (case 3 in Table 1) is shifted toward the tensile side with respect to that of the first generation (case 6 in Table 1). Besides the different nature of the residual stress field (tensile versus compressive in third- and first-generation implants, respectively), completely different topological patterns were also revealed. A finer periodicity could be observed in the third-generation material with finer microstructure [Fig. 7(B)] with respect to the coarse-grained material of the first-generation implant [Fig. 7(D)]. Note that the fine residual stress patterns shown in Figs. 7(B) and 7(D) could be recorded only by adopting the confocal probe configuration. On the other hand, the spectral convolution involved with probing subsurface portions of the sample in nonconfocal assessment led to significantly low stress magnitudes and, thus, could not reveal any tangible stress pattern on the surface.

4.3 *Micromechanisms of Wear Damage in Al_2O_3 Hip Joints*

In the previous section, we proved the capability of a confocal optical microprobe in revealing with high spatial resolution of both surface and subsurface residual stress fields in retrieved Al_2O_3 hip joints. These preliminary results, obtained with high statistical reliability, can be considered encouraging; but they are insufficient to draw a final conclusion on the mechanisms behind wear degradation in Al_2O_3 hip joints. In particular, in this study, all the short-term exposed prostheses belonged to the third-generation Al_2O_3 joints and all the long-term exposed prostheses belonged to the first generation. In other words, the short-term residual stress patterns developed in the first-generation and the long-term patterns developed in the third-generation prostheses could not be retrieved. Therefore, the plot in Fig. 6 of residual stress versus exposure time *in vivo* necessarily represents an extrapolation of the actual time-dependent residual stress behavior of Al_2O_3 artificial hip joints. Despite this limitation, we can propose hereafter only a simplified model for explaining the time-dependence plot in Fig. 6. A schematic of the interaction between the surfaces of acetabular cup and femoral head on the microstructural level is shown in Fig. 8. In the early period of implantation lifetime, the surface of the femoral head is subjected to significant local impingement arising from severe microseparation phenomena in the hip joint [Fig. 8(A)]. As a consequence of local impingements, intergranular microcracking will take place and will later develop into debris formation in main-wear zones [Fig. 8(B)]. Cracking, which is a consequence of local shocks and point forces, can introduce in the surface a residual stress field of tensile nature. Cracks selectively develop at Al_2O_3 grain boundaries where the stress intensification is higher.[24,25] Grain-size-related stress intensification in polycrystalline materials has been shown to increase with increasing grain size.[25,26] Therefore, the tensile residual stress field may develop faster and with higher magnitude in coarse-grained Al_2O_3 hip prostheses than in fine-grained materials. Microcracking will successively develop into grain spalling [Fig. 8(B)] and detachment [Fig. 8(C)], with subsequent development of ceramic debris. This stage should be accompanied by a release of the tensile residual stress field. The compressive residual stresses stored on the ceramic joint surface are the consequence of long-term impingements assisted by third bodies (i.e., the ceramic debris). This latter stress field was described in the previous section as arising from loading history and it increases with increasing exposure time *in vivo* up to a saturation value, above which more extensive detachment occurs and abraded areas (stripe-wear zones[9,10,27]) may develop.

5 Conclusion

After systematically evaluating the probe response functions of the chromophoric fluorescence spectrum of Al_2O_3 polycrystals with different grain sizes as constituent materials for artificial hip joints, a suitable confocal probe configuration could be identified, which enabled us to greatly reduce laser penetration depth in the material. By scanning with the focal plane either on the surface or 30 μm below it in the subsurface of the material, residual stress fields in retrieved Al_2O_3 hip joints could be systematically evaluated. *In toto* residual stress maps were clearly related to the existence of main wear zones on the joint surface and clarified the stress equilibrium conditions between surface and subsurface. The microscopic stress distributions on the surface of wear zones of third- and first-generation Al_2O_3 femoral heads were also retrieved and analyzed in detail with micrometric resolution. They revealed distinctly different stress patterns between Al_2O_3 joints after short-term and long-term exposure *in vivo*. These patterns could not be observed in nonconfocal probe configuration because of severe convolution of the highly graded subsurface residual stress field. This paper clearly shows the suitability of confocal fluorescence PS for systematic wear studies of Al_2O_3 hip joints; however, it leaves unanswered such important issues as the role of grain size on the wear response of the ceramic surface and, thus, on the actual lifetime of the joint. These issues can be further evaluated by PS assessments of hip joints on systematically loading them for increasing times in advanced simulator devices, including microseparation effects.

Acknowledgments

The authors sincerely acknowledge Prof. I. C. Clarke for his useful discussions on the tribological behavior of alumina hip joints. Prof. L. Sedel and Dr. G. Falcone are sincerely acknowledged for making available to us the alumina hip retrievals. Mr. K. Wan and Mr. S. Tochino are acknowledged for their useful discussions on the probe response function and PS calibrations of polycrystalline alumina.

References

1. J. Pawley, *Handbook of Biological Confocal Microscopy*, 2nd ed., Plenum, New York (1995).
2. J. M. Schmitt, A. Knuttel, and M. Yadowsky, “Confocal microscopy in turbid media,” *J. Opt. Soc. Am. A* **11**, 2226–2235 (1994).
3. G. Pezzotti and A. A. Porporati, “Raman spectroscopic analysis of phase-transformation and stress patterns in zirconia hip joints,” *J. Biomed. Opt.* **9**, 372–384 (2004).
4. G. Pezzotti, “Raman piezo-spectroscopic analysis of natural and synthetic biomaterials,” *Anal. Bioanal. Chem.* **381**, 577–590 (2005).
5. I. C. Clarke, G. Pezzotti, S. Sakakura, and B. Ben-Nissan, “Biolubrication phenomena affect residual stresses and phases of zirconia implants,” *Key Eng. Mater.* **240–242**, 781–784 (2003).
6. H. Mittelmeier and J. Heisel, “Sixteen-years’ experience with ceramic hip prostheses,” *Clin. Orthop. Relat. Res.* **282**, 64–72 (1992).
7. P. Boutin, P. Christel, J.-M. Dorlot, A. Meunier, A. de Roquancourt, D. Blanquaert, S. Herman, L. Sedel, and J. Witvoet, “The use of dense alumina-alumina ceramic combination in total hip replacement,” *J. Biomed. Mater. Res.* **22**, 1203–1232 (1988).
8. J. Nevelos, E. Ingham, C. Doyle, J. Fisher, and A. B. Nevelos, “Examination of retrieved alumina ceramic components from Mittelmeier total hip prostheses,” *Biomaterials* **20**, 1833–1840 (1999).
9. T. Shishido, I. C. Clarke, P. Williams, M. Boehler, T. Asano, H. Shoji, T. Masaoka, K. Yamamoto, and A. Imakiire, “Clinical and simulator wear study of alumina THR to 17 years and beyond,” *J. Biomed. Mater. Res.* **67B**, 638–647 (2003).
10. M. Manaka, I. C. Clarke, K. Yamamoto, T. Shishido, A. Gustafson, and A. Imakiire, “Stripe wear rates in alumina THR—comparison of microseparation simulator study with retrieved implants,” *J. Biomed. Mater. Res.* **69B**, 149–157 (2004).
11. L. Grabner, “Spectroscopic technique for the measurement of residual stress in sintered Al_2O_3,” *J. Appl. Phys.* **49**, 580–583 (1978).
12. J. He and D. R. Clarke, “Determination of the piezospectroscopic coefficients for chromium-doped sapphire,” *J. Am. Ceram. Soc.* **78**, 1347–1353 (1995).
13. Q. Ma and D. R. Clarke, “Piezospectroscopic determination of residual stresses in polycrystalline alumina,” *J. Am. Ceram. Soc.* **77**, 298–302 (1994).
14. L. Colombi Ciacchi, G. Gregori, V. Lughi, A. Rossi, and V. Sergo, “Piezo-spectroscopy: a materials science perspective,” in *Recent Research Developments in Applied Spectroscopy*, Vol. **2**, pp. 243–272, S. G. Pandalai, Ed., Research Signpost, Kerala, India (1999).
15. D. M. Lipkin and D. R. Clarke, “Sample-probe interactions in spectroscopy: sampling microscopic property gradients,” *J. Appl. Phys.* **77**, 1855–1863 (1995).
16. A. Atkinson and S. C. Jain, “Spatially resolved stress analysis using Raman spectroscopy,” *J. Raman Spectrosc.* **30**, 885–891 (1999).
17. *MATHEMATICA4*, Wolfram Research, Inc.
18. E. Gaudry, A. Kiratisin, P. Sainctavit, C. Brouder, F. Mauri, A. Ramos, A. Rogalev, and J. Goulon, “Structural and electronic relaxation around substitutional Cr^{3+} and Fe^{3+} ions in corundum,” *Phys. Rev. B* **67**, 094108–094116 (2003).
19. A. R. Blak, V. Gobbi Jr., and F. Ayres, “Dipole defects in Al_2O_3:Mg,Cr,” *Radiat. Prot. Dosim.* **100**, 67–70 (2002).
20. H. Yu and D. R. Clarke, “Effect of codoping on the R-line luminescence of Cr^{3+}-doped alumina,” *J. Am. Ceram. Soc.* **85**, 1966–1970 (2002).
21. D. S. McClure, “Electronic structure and spectra of impurities,” in *Treatise in Solid State Chemistry*, Vol. **2**, N. B. Hannay, Ed., pp. 1–132, Plenum Press, New York (1988).
22. D. S. McClure, “Optical spectra of transition metal ions in corundum,” *J. Chem. Phys.* **36**, 2757–2779 (1962).
23. Q. Ma and D. R. Clarke, “Stress measurement in single and polycrystalline ceramics using their optical fluorescence,” *J. Am. Ceram. Soc.* **76**, 1433–1440 (1993).
24. D. R. Clarke, “Microfracture in brittle solids resulting from anisotropic shape changes,” *Acta Metall.* **28**, 913–924 (1980).
25. V. Tvergaard and J. W. Hutchinson, “Microcracking in ceramics induced by thermal expansion or elastic anisotropy,” *J. Am. Ceram. Soc.* **71**, 157–166 (1988).
26. F. J. P. Clarke, “Residual strain and fracture stress-grain size relationships in brittle solids,” *Acta Metall.* **12**, 139–142 (1964).
27. T. Tateiwa, I. C. Clarke, H. Shirasu, G. Pezzotti, L. Sedel, T. Masaoka, T. Shishido, and K. Yamamoto, “Surface micro-analyses of long-term worn retrieved ‘Osteal™,’ alumina ceramic THR,” *J. Biomed. Mater. Res., Part B: Appl. Biomater.* (in press).